

Sub-band Digital Predistortion for Noncontiguous Transmissions: Algorithm Development and Real-Time Prototype Implementation

Mahmoud Abdelaziz¹, Chance Tarver², Kaipeng Li², Lauri Anttila¹, Raul Martinez²,
Mikko Valkama¹, and Joseph R. Cavallaro²

¹Department of Electronics and Communications Engineering, Tampere University of Technology, Tampere, Finland

²Department of Electrical and Computer Engineering, Rice University, Houston, TX

Abstract—This article proposes a novel, reduced complexity, block-adaptive digital predistortion (DPD) technique for mitigating the spurious emissions that occur when amplifying spectrally noncontiguous signals with a nonlinear power amplifier (PA). The introduced DPD solution is designed for real-time scenarios where a loop delay exists in the DPD system. By a proper choice of the DPD parameters, the technique is shown to be robust against arbitrarily long loop delays while not sacrificing DPD linearization performance and convergence speed. Moreover, the proposed DPD solution has lower complexity compared to previously proposed solutions in the literature while giving excellent linearization performance in terms of mitigating the spurious emissions. Real-time implementations of the algorithm on the WARP platform are developed, including considerations for several key trade-offs in the hardware design to balance the robustness, performance and complexity. The simulations and real-time FPGA experiments evidence excellent and robust performance in real-life situations with highly nonlinear PAs and arbitrary loop delays.

Index Terms—carrier aggregation, digital predistortion, dynamic spectrum access, FPGA, LTE-A, noncontiguous spectrum transmission, power amplifier nonlinearity, real-time implementation.

I. INTRODUCTION

DIGITAL predistortion (DPD) is one of the most effective solutions for transmitter linearization, and has attracted substantial attention in the past 15-20 years (see [1] and the references therein). The vast majority of the previous works on DPD has concentrated on single-carrier transmissions. However, noncontiguous spectral allocations are gradually becoming a norm in many wireless communication standards, such as 3GPP LTE-A and the 802.11 family. In scenarios where a single power amplifier (PA) is used to amplify several component carriers (CCs), two challenges arise for the DPD design: (1) The introduction of intermodulation distortion

(IMD) between the noncontiguous CCs, which may lead to a violation of the transmitter emission masks [2], [3] as shown in Fig. 1, and (2) the increased DPD parameter estimation and filtering complexity, especially when the spacing between the CCs is large. This comes as a result of the DPD processing and estimation generally having to operate at a sample rate of at least five times the overall aggregated bandwidth (the allocated bandwidth plus the CC separation). Consequently, the DPD complexity and power consumption quickly rise, and the additional complexity due to DPD may become unjustifiable, especially for mobile-like devices.

In [4] and [5] a new DPD solution has been proposed that can tackle the IMD resulting from noncontiguous bandwidth allocations with a significantly lower complexity compared to previous solutions. This DPD solution focuses on mitigating certain IMD spurs only, which in many scenarios are the limiting factor in terms of transmitter emission violations, especially for portable devices [2], [3]. The idea is based on injecting IMD spurs with opposite phase into the input of the PA, such that at the output of the PA the spur is cancelled. This idea of IMD spur injection was previously introduced in [6]–[8], where frequency-flat PA responses were assumed within the spurious bands. On the other hand, the DPD learning in [5] was based on a lower complexity online adaptive decorrelation between locally generated baseband nonlinear basis functions representing the IMD at the target sub-band, and the actual IMD spur at the PA output. The PA frequency selectivity was also taken into consideration, thus giving better results compared to previous solutions. The main advantage of this spur injection DPD approach, which we refer to as “sub-band DPD”, compared to traditional DPD methods, which aim to linearize the whole aggregated transmit band (“full-band DPD”), is the significant reduction in the complexity in both the DPD processing and estimation stages. The main scope of this article is to develop and modify the algorithm from [5] to be more suitable to real-time implementation with arbitrary loop delay, as well as to develop a real-time hardware prototype for the DPD solution on the WARP platform.

The challenges associated with real-time implementation, in particular the loop time delay, require a modification of the DPD design on the system level. A new block-adaptive

This work was supported by the Finnish Funding Agency for Technology and Innovation (Tekes) under the projects “Cross-Layer Modeling and Design of Energy-Aware Cognitive Radio Networks (CREAM)”, and “Future Small-Cell Networks using Reconfigurable Antennas (FUNERA)”. The work was also funded by the Academy of Finland under the projects 251138 “Digitally-Enhanced RF for Cognitive Radio Devices” and 284694 “Fundamentals of Ultra Dense 5G Networks with Application to Machine Type Communication”, and by the Linz Center of Mechatronics (LCM) in the framework of the Austrian COMET-K2 programme. This work was also supported in part by the US National Science Foundation under grants CNS-1265332.

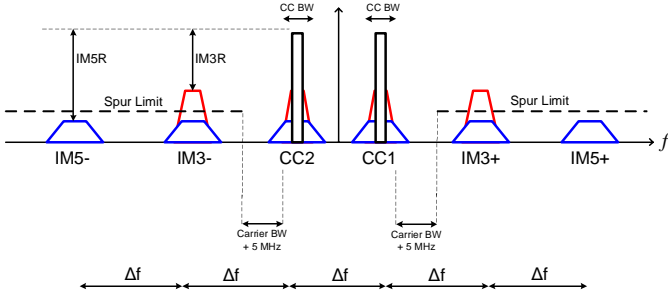


Fig. 1. Intermodulation spurs created by the nonlinear PA due to noncontiguous transmission with two component carriers.

DPD solution, opposed to the earlier sample-adaptive solution in [4], [5], is introduced in this paper. A real-time software implementation of the proposed block-adaptive sub-band DPD algorithm is presented. In addition, an FPGA implementation is also developed, with even lower complexity and power consumption, and less delay constraints compared to the software implementation. We show that the proposed solution can act as a cost effective and efficient DPD solution for wireless portable devices with limited processing capabilities.

The rest of the article is organized as follows: Section II introduces the new block-adaptive sub-band DPD learning algorithm. In Section III, computational and instrumentation complexity of sub-band vs. full-band DPD are discussed. Section IV shows some simulation examples. Section V explains the prototype implementation platform with a real WLAN RF transceiver and the implementation results for the proposed DPD solution. Finally, Section VI concludes the main findings in this paper.

II. BLOCK-ADAPTIVE DECORRELATION-BASED SUB-BAND DPD SOLUTION

The output of a third-order PA model when excited with a noncontiguous signal is shortly analyzed at composite baseband equivalent level, assuming a parallel Hammerstein (PH) model for the PA. The two CCs are assumed to be separated by Δf as shown in Fig. 1. Thus, the composite baseband equivalent PA input and output signals, $x(n)$ and $y(n)$, read

$$x(n) = x_1(n)e^{j2\pi\frac{\Delta f}{2f_s}n} + x_2(n)e^{-j2\pi\frac{\Delta f}{2f_s}n} \quad (1)$$

$$y(n) = f_{1,n} \star x(n) + f_{3,n} \star |x(n)|^2 x(n), \quad (2)$$

where $f_{1,n}$ and $f_{3,n}$ are the filters in the main and third order PH branches, respectively, \star is the convolution operator, and $x_1(n)$ and $x_2(n)$ are the baseband equivalents of the input CCs. Through direct substitution of (1) in (2), the baseband equivalent positive IM3 term, as an example, can be easily extracted, yielding

$$y_{IM3+}(n) = f_{3,n}^{3+} \star (x_2^*(n)x_1^2(n)). \quad (3)$$

Here, $f_{3,n}^{3+}$ is the baseband equivalent response of $f_{3,n}$ at the positive IM3 sub-band around $(f_c + 3\Delta f/2)$, where f_c denotes the carrier frequency. Stemming from the signal structure in (3), a natural injection signal is a filtered version of the basis function $x_2^*(n)x_1^2(n)$ using a filter α_n with memory depth N .

Incorporating such DPD processing, the composite baseband equivalent PA input signal $\tilde{x}(n)$ reads

$$\tilde{x}(n) = x(n) + [\alpha_n^* \star (x_2^*(n)x_1^2(n))] e^{j2\pi\frac{3\Delta f}{2f_s}n}. \quad (4)$$

Substituting now $\tilde{x}(n)$ in (2), the positive IM3 sub-band signal at the PA output becomes

$$\begin{aligned} \tilde{y}_{IM3+}(n) \approx & (f_{3,n}^{3+} + f_{1,n}^{3+} \star \alpha_n^*) \star x_2^*(n)x_1^2(n) \\ & + 2f_{3,n}^{3+} \star (|x_1(n)|^2 + |x_2(n)|^2)(\alpha_n^* \star x_2^*(n)x_1^2(n)), \end{aligned} \quad (5)$$

where terms with nonlinearity order higher than five have been neglected for simplicity of presentation. From (5), it can be shown that the strength of the considered IM3 sub-band signal at the PA output depends directly on, and can thus be controlled by, the DPD filter α_n . Examining the first line of (5), it can be seen that the solution that nulls the third order term is simply obtained by setting the first line of the equation to zero, i.e., $f_{3,n}^{3+} + f_{1,n}^{3+} \star \alpha_n^* = 0, \forall n$. This solution is called the *third order inverse solution*.

However, the IM3 sub-band signal always contains higher order IM products, created by the PA nonlinearity and the predistortion itself, such as the fifth order term seen on the second line of (5). The third order inverse solution cannot suppress these higher order components. Meanwhile, the fifth order term can be seen to be strongly correlated with the third order basis function, $x_2^*(n)x_1^2(n)$. We therefore conjectured, as showed in [4], [5], that *decorrelating* the IM3 sub-band signal at the PA output with $x_2^*(n)x_1^2(n)$ and its delayed replicas could give superior performance compared to the third order inverse solution. The DPD filter coefficients will converge to the value that minimizes the correlation between the measured signal at the target IM3 sub-band and the corresponding basis function, thus achieving the objective of suppressing the power in the IM3 sub-band.

A challenging problem appears when implementing this DPD solution on a real-time platform. During the DPD learning phase, and under real time constraints the DPD parameter convergence and consequently the DPD linearization performance can be affected if the learning loop delay becomes large. Stemming from these real time challenges, a new block-adaptive decorrelation-based sub-band DPD solution is developed in this work. A block diagram explaining the main architecture of the proposed block based solution is shown in Fig. 2. For further algorithm flexibility and delay tolerance compared to the sample-adaptive techniques in [4], [5], we introduce a block-adaptive learning rule with two distinct block definitions as illustrated in Fig. 3. A single update of the algorithm will utilize M samples, as shown in (6), whereas the DPD parameter update interval is L samples, with $M \leq L$. Thus, by proper choice of M and L , arbitrarily long loop delays can be tolerated, facilitating real-time implementation.

Based on the DPD architecture in Fig. 2, and the block-based learning in Fig. 3, and assuming an estimation block size of M samples, and $N + 1$ DPD filter coefficients, the

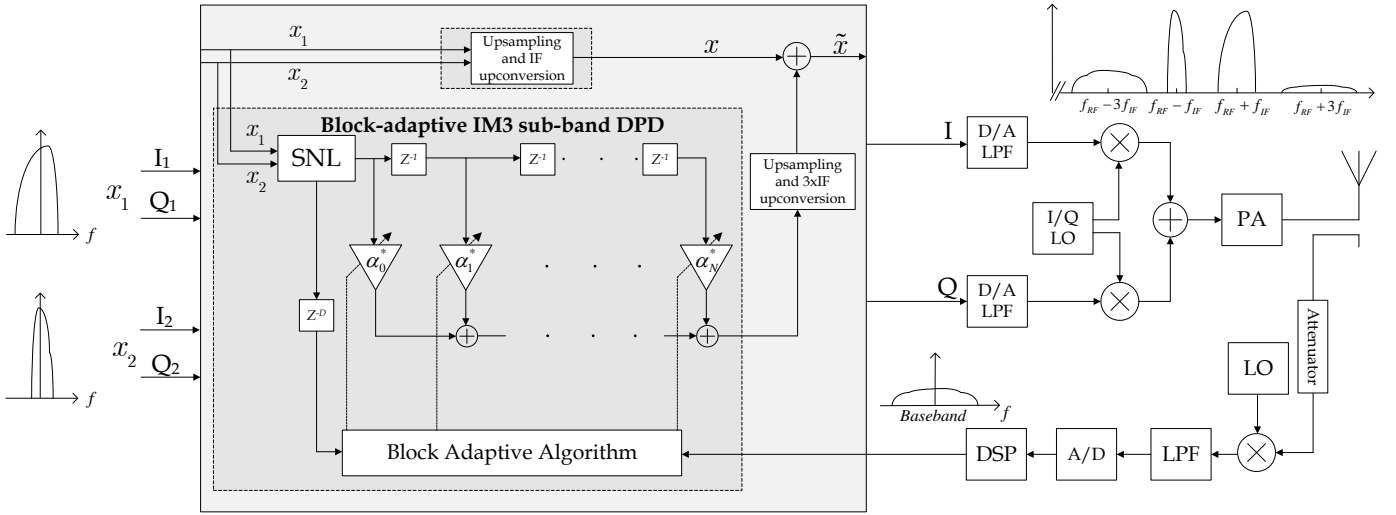


Fig. 2. Block-adaptive decorrelation-based sub-band DPD system architecture for third-order spurious intermodulation reduction in a noncontiguous transmitter. Also essential composite baseband equivalent spectra are shown. The static nonlinearity (SNL) block generates the third order basis function for the IM3 sub-band.

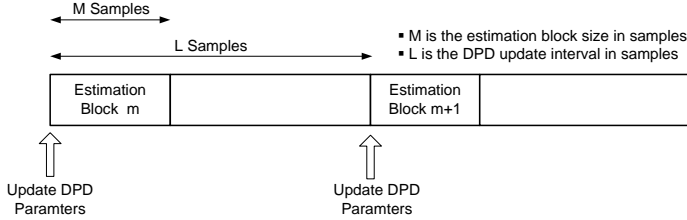


Fig. 3. Block based DPD learning concept. The DPD parameter(s) estimated in the current estimation block m are applied on the next block.

DPD parameter learning algorithm becomes

$$\alpha(m+1) = \alpha(m) - \frac{\mu}{\|\mathbf{U}(m)\|^2 + C} [\mathbf{e}^H(m)\mathbf{U}(m)]^T, \quad (6)$$

where

$$e(n) = \tilde{y}_{IM3+}(n) \quad (7)$$

$$\mathbf{e}(m) = [e(n_m) \ e(n_m+1) \ \dots \ e(n_m+M-1)]^T \quad (8)$$

$$u(n) = x_2^*(n)x_1^2(n) \quad (9)$$

$$\mathbf{u}(n_m) = [u(n_m) \ u(n_m+1) \ \dots \ u(n_m+M-1)]^T \quad (10)$$

$$\mathbf{U}(m) = [\mathbf{u}(n_m) \ \mathbf{u}(n_m-1) \ \dots \ \mathbf{u}(n_m-N)] \quad (11)$$

$$\alpha(m) = [\alpha_0(m) \ \alpha_1(m) \ \dots \ \alpha_N(m)]^T. \quad (12)$$

Here, $\tilde{y}_{IM3+}(n)$ is the positive IM3 signal measured from the PA output, $\mathbf{e}(m)$ is the error signal vector, and $\mathbf{U}(m)$ is the filter input matrix, with m denoting the block index. The index of the first sample of block m is denoted by n_m . The DPD filter $\alpha(m)$ is applied on the whole block of L samples as illustrated in Fig. 3.

III. COMPUTATIONAL AND HARDWARE COMPLEXITY PERSPECTIVES

In this section, we provide a more thorough comparison of the computing and hardware complexities of the sub-band

DPD introduced in this paper which focuses on a specific IM sub-band and the conventional full-band DPD architecture.

A. Sample Rate and Parameter Number Considerations

The full-band DPD, assuming nonlinearity order seven, needs to run at a sample rate seven times the composite dual-carrier signal bandwidth, which quickly becomes impossible when the carrier separation increases. For the sub-band technique, on the other hand, the minimum sample rate is less than or equal to three times the bandwidth of the wider component carrier for a third order sub-band DPD as proposed in this article. Simulation results in section IV show that a third order sub-band DPD has a similar if not better performance than a seventh order full-band DPD in terms of spurious emission suppression. This is the motivation for using these DPD orders in the comparison. To give a more concrete example, let us assume two 5 MHz CCs separated by 30 MHz. The minimum sample rate with a classical seventh order full-band DPD would be 245 MHz, whereas with the third order sub-band DPD, it is only 15 MHz. The difference in complexity becomes even bigger when higher order DPDs are considered and/or the carrier spacing between the two CCs is increased.

Frequency selectivity of the nonlinear PA is another important factor to be considered when comparing the two DPD architectures. The full-band DPD predistorts the whole aggregated band, which in our previous example is almost an order of magnitude bigger than the IM3 sub-band predistorted by the sub-band DPD. This implies that when memory effects of the PA are considered, substantially longer filters are needed in the full-band DPD compared to the sub-band DPD, to reach a certain performance requirement. In the experiments in this paper (see Section IV and V), only a single tap is used in the sub-band DPD, while still providing comparable spur mitigation performance when compared to a multi-tap

full-band DPD.

B. Running Complexity

In general, the computational complexity of the DPD can be classified into three main parts [9]: identification complexity, adaptation complexity, and running complexity. The identification part is basically the estimation complexity of the DPD parameters, while the adaptation complexity includes the required processing by the DPD in order to adapt to new operating conditions or device aging. Finally, the running complexity, which is the most critical especially for mobile-type devices, involves the number of computations done per second while the DPD is operating.

To get a more quantitative understanding of the computational running complexity difference between the full-band and sub-band DPD architectures, we shall use the number of floating point operations (FLOPs) per sample, the number of DPD parameters, and the required sample rate in the predistortion path as quantitative metrics. The running complexity is divided into two main parts, (1) the basis function generation and (2) the actual predistortion using these basis functions [9]. The full-band DPD architecture that we use in our comparative performance simulations, and which is also widely applied otherwise, is based on the parallel Hammerstein (PH) architecture polynomial basis functions and FIR filters [1]. Considering a seventh order PH architecture with memory order three, 9 FLOPs are required for the basis functions generation [9]. The predistortion filtering requires 4×3 complex multiplications and additions with eight FLOPs each (i.e. 96 FLOPs). Thus the total number of FLOPs required by the full-band DPD in this particular example is 105 FLOPs per output sample.

In the sub-band DPD, on the other hand, when the positive IM3 sub-band is considered for example, the third order basis function reads $x_2^*(n)x_1^2(n)$ [4], requiring only two complex multiplications with 6 FLOPs each. Consequently, the number of FLOPs required by the sub-band DPD for basis function generation is 12 FLOPs per sample per sub-band. Moreover, in the sub-band DPD architecture, a single tap is shown to be enough to achieve satisfactory intermodulation suppression as shown in the simulation and implementation examples in sections IV and V, when compared to the full-band DPD. Thus, a single complex multiplication, or 6 FLOPs, is required per sample per processed sub-band for the sub-band DPD filtering. The total number of FLOPs required by the sub-band DPD in our example thus becomes 18 FLOPs. Based on these numbers, and taking into account the required sample rates in the scenario with two 5 MHz CCs and 30 MHz carrier spacing, the number of FLOPs per second (FLOPS) becomes 25.725 GFLOPS for the full-band DPD, and 0.27 GFLOPS for the sub-band DPD. These numbers are summarized in Table I.

C. Feedback Receiver Instrumentation Complexity

In addition to the complexity reduction in the DPD main path, the complexity of the feedback path used for DPD parameter estimation and adaptation is also greatly reduced.

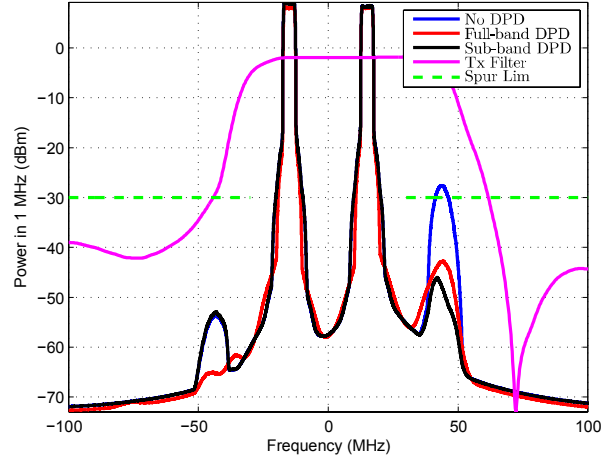


Fig. 4. Dual-carrier mobile transmitter baseband equivalent power spectra. The full-band and sub-band DPDs are compared to not using DPD at all. Each CC is allocated 5 MHz with 20 dBm total output power, using a PH PA model extracted from actual RF measurements.

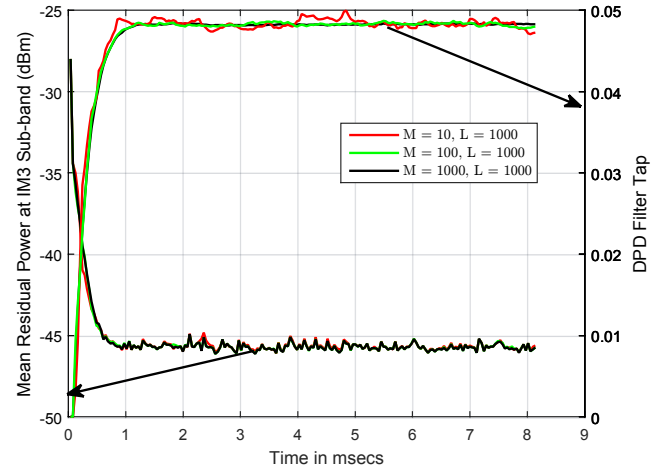


Fig. 5. The convergence of the DPD filter tap along with the mean residual power in the positive IM3 sub-band for different values of M and L.

In order to estimate the parameters of the positive IM3 sub-band DPD, as an example, we only need to observe the positive IM3 sub-band at the PA output in order to estimate the DPD parameters, instead of observing the whole signal band (including the IM sub-bands), which is the case with full-band DPD. This reduction in the observation bandwidth reduces the cost, complexity, and power consumption in the feedback path, thus allowing use of simpler instrumentation.

IV. SIMULATION RESULTS

A carrier aggregated LTE-A uplink signal with QPSK subcarrier modulation is applied to a wide-band parallel Hammerstein PA model of nonlinearity order 5, which is based on measurements of a real mobile PA. The carrier separation between the two CCs is 30 MHz, and a duplexer filter model

TABLE I
 QUANTITATIVE RUNNING COMPLEXITY AND LINEARIZATION PERFORMANCE COMPARISON OF FULL-BAND VERSUS SUB-BAND DPD. 5 MHz BW ALLOCATION PER CC WITH 30 MHz CARRIER SPACING IS USED AS IN FIG. 4.

	DPD Running Complexity			Performance	
	Coeffs	Fs [MSPS]	GFLOPS	EVM [%]	Positive IM3R [dBc]
No DPD	N/A	N/A	N/A	2.1916	31.2181
Full-Band DPD	12	245	25.725	0.3699	44.5674
Sub-Band DPD	1	15	0.27	2.2519	50.2562

based on a real mobile duplexer is also used in our simulations. The bandwidth of each CC is 5 MHz, and the carriers are allocated such that the positive IM3 sub-band lies close to the edge of the transmitter filter passband. Our proposed block adaptive sub-band DPD is then tuned to predistort the positive IM3 sub-band since the negative one is already filtered by the transmitter filter as shown in Fig. 4. In this example, the estimation block size $M = 100$, while the DPD update interval $L = 1000$, and a single sub-band DPD filter coefficient is used. Fig. 5 shows the convergence of the sub-band DPD filter coefficient and the mean residual power in the IM3 sub-band for different configurations of the DPD estimation block size M and update interval L . The figure shows the reliability of the sub-band DPD performance even when the difference between M and L gets larger, which means larger tolerance for additional loop delay in the system.

In the full-band DPD scenario, implemented for reference, a seventh order DPD based on the indirect learning architecture (ILA) (see [1]) is used. Altogether four filters, all with 3 taps, are used in the full-band DPD, one for each basis function. Three ILA iterations are used. In the full-band DPD, an inherent 1.5 dB backoff needs to be applied to the transmit path to account for the slight increase in the PAPR due to the predistortion, something which is not needed in the sub-band DPD. Therefore, for a fair comparison, the transmitter power levels are adjusted such that the output power after the PA is the same for both full-band and sub-band DPDs.

In Fig. 4, the Tx power level is 20 dBm, and it can be seen that without applying DPD, the transmitter violates the spurious emission limit of -30 dBm/MHz, defined by ITU-R [10]. After the DPD, the spur levels are below the limit with both DPD architectures. Table I shows a quantitative complexity and performance analysis of the full-band and sub-band DPDs used in Fig. 4. The complexity numbers were already treated in Section III. To recap, the number of FLOPs per second (FLOPS) is 25.725 GFLOPS for the full-band DPD, and 0.27 GFLOPS for the sub-band DPD, evidencing remarkable complexity and power consumption savings with the sub-band DPD architecture. In terms of linearization performance, both DPDs give quite good suppression for the IM3 distortion. We quantify the suppression of intermodulation power at the IM3 bands through the power ratios relative to the component carrier wanted signal power as shown in Fig. 1, and defined as

$$IM3R_{dB} = 10 \log_{10} \frac{P_{wanted,cc}}{P_{IM3}} \quad (13)$$

The IM3R at the positive IM3 sub-band, without any Tx

filter, is shown in Table I for the CC allocations in Fig. 4. The sub-band DPD provides a slightly better performance in terms of the positive IM3R compared to the full-band DPD in this particular scenario. The inband distortion (Error Vector Magnitude; EVM) is also measured, where the full-band DPD somewhat outperforms the sub-band DPD. This is expected, since the full-band DPD considers the whole transmit band including the main component carriers. However, the EVM degradation with the sub-band DPD as compared to without DPD is around 0.06%, which is negligible.

V. EXPERIMENTAL TESTING AND RESULTS

In this section, we illustrate two schemes on experimental verification of DPD functionalities, including a WARPLab-based fast prototyping and a FPGA-based real-time implementation. Corresponding results are also shown for each scheme.

A. Experimental Verification based on WARPLab

The functionality of the block based DPD design is verified experimentally using the WARPLab framework and the Wireless Open Access Research Platform (WARP) v3 board. WARPLab is a software-defined radio framework for rapid PHY prototyping. WARPLab consists of a commercial PC for baseband processing in MATLAB, WARP radio nodes for signal transmitting or receiving, and an Ethernet link for transferring data and commands between PC and WARP nodes. For further details on WARPLab and the WARP boards, see [11].

The experimental setup for testing the block based digital predistortion algorithm with a real power amplifier is as follows. A signal for broadcasting is generated in MATLAB. A block is sent to the WARP board using WARPLab version 7.5.1. The signal is transferred through the transmit path of the hardware which includes a digital to analog converter, up-conversion to 2.4 GHz, amplification, and transmission through a SMA connector on the RF port A to coax. The signal passes through 40 dB of in-line attenuation to protect the receive path and is then received on the RF port B of the same board. The signal is down-converted and sampled via an ADC. Samples are stored in a buffer and then sent through the ethernet cable back to the computer for processing in MATLAB. The frame synchronization of input and output is performed by inserting long training sequence (LTS) preamble at input frames and detecting correlation peaks at output frames. Based on the processing of the received block, a DPD coefficient update is calculated as in (6) such that the next filtering block can be predistorted using the new α . This process continues iterating until α converges.

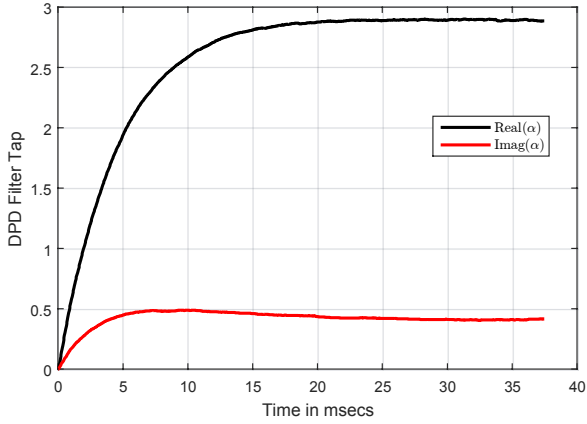


Fig. 6. Convergence of DPD filter coefficient α in the WARPLab experiment.

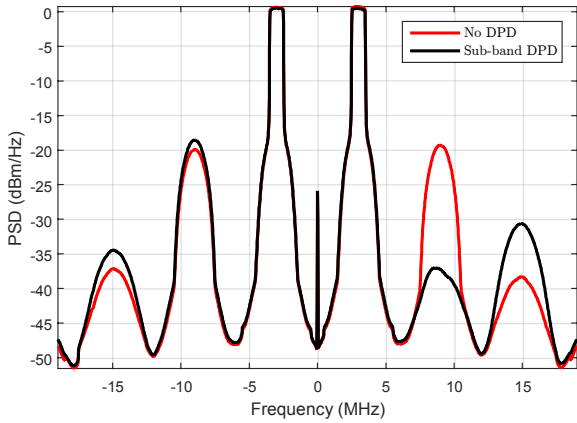


Fig. 7. Power spectral density with and without DPD of WARPLab Experiment shown here at baseband with approximately 18 dB of suppression at the IM3 sub-band.

B. WARPLab Results

For the WARPLab testing, a carrier aggregated LTE-A uplink signal with QPSK subcarrier modulation is used. The carrier separation is 6 MHz. The bandwidth of each CC is 1.4 MHz. The memoryless, single-tap block-adaptive sub-band DPD is used. For the results presented here, the estimation block is of length $M = 528$, and the DPD update interval $L = 1024$.

The convergence of the DPD coefficient α is shown in Fig. 6. The real and imaginary parts both converge quickly and smoothly. In Fig. 7 the spectrum is shown when broadcasting with the final, converged coefficients from Fig. 6. Comparing this to the red spectrum where no DPD is used, the result shows 18 dB reduction in the positive IM3 spurious emission. Note that here we did not use a transmitter filter to filter out the negative IM3 spurious spectrum as the MATLAB simulation results in Fig. 4 for simplicity. Certainly we can apply the same DPD algorithm to suppress the negative IM3 spurious emission as well.

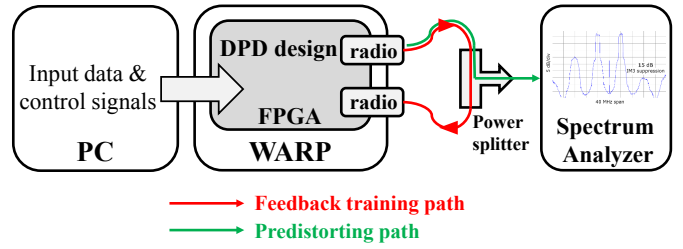


Fig. 8. Experimental setup for real-time FPGA testing.

C. Real-time FPGA Implementation

We further implement our block-based, sub-band DPD design on a Xilinx Virtex 6 FPGA to support real-time DPD processing on actual mobile devices. The block-based DPD architecture as highlighted in Fig. 2 is mapped and implemented in the FPGA fabric of the WARP board. The memoryless, single-tap, block-based DPD design is used. It is developed using the Xilinx System Generator tools as an IP core that could potentially be added to any wireless system design.

The FPGA design has a loop delay of approximately 80 clock cycles. For the design, the estimation block size $M = 256$, and $L = 512$ is the DPD update interval. This choice in block lengths is short enough to facilitate rapid convergence, and the difference between the filtering block size and the learning block is greater than the loop delay as required for proper convergence. The lengths of the blocks are controlled via counters and powers of two were chosen to ease computational complexity.

To compute the DPD coefficient update in (6), a complex multiplication between the conjugate of the error samples and the third order IM3 basis function samples is continuously performed during the estimation block. The result of this is accumulated and a right bit shift is used to approximate the normalization scaling in (6). At the end of the estimation block a subtraction is enabled and then the accumulator is reset until the next estimation block.

The experimental setup for performing real-time testing of the FPGA design is shown in Fig. 8. It is similar to the WARPLab setup described earlier. However, MATLAB is not used to control the design and do the processing. Instead, the computer is only used for sending control signals such as enable and reset to the FPGA via the USB-UART communication port.

D. Real-time FPGA Results

For the FPGA design testing, a carrier aggregated LTE-A uplink signal with QPSK subcarrier modulation generated in MATLAB was stored in the block RAM (BRAM) of the FPGA for testing. The carrier separation is 6 MHz. The bandwidth of each CC is 1.4 MHz.

In Fig. 9, we see how the convergence of the DPD coefficient α behaves. In this figure, the FPGA design shows rapid convergence of α and remains relatively constant. A spectrum analyzer was used to view the spectrum for the

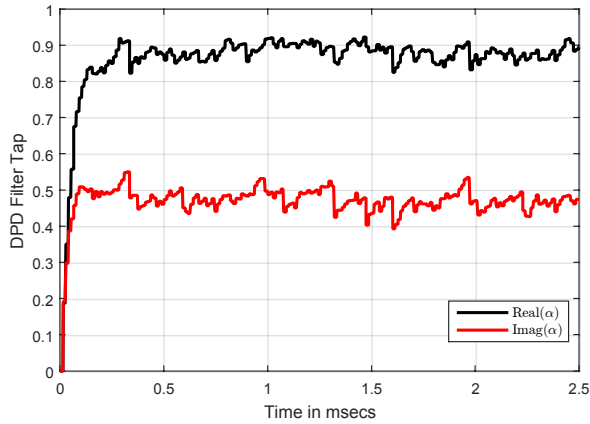


Fig. 9. Convergence of DPD filter coefficient α in the FPGA hardware implementation of the block-based sub-band DPD.

FPGA design. The spectrum analyzer output with and without DPD is shown in Fig. 10. This figure shows the results at Wi-Fi channel 6 (2.437 GHz) where the WARP board operates for the experiment. These results show a 12 dB reduction in the positive IM3 spurious emission.

Most of the multiplications in the architecture are done in specialized hardware multiplier units of the Virtex 6 known as DSP48E1 slices. When generated, the DPD module uses a total of 242 DSP48E1 slices out of the 768 available DSP48E1 slices. Of this, many are being used by an order 100 FIR filter to extract a block of the IM3 spurious emission samples $\tilde{y}_{IM3,+}(n)$ at the PA output, which represent the block of error samples as indicated in (7) and (8). Currently the FPGA design focuses on performance. For better performance/utilization tradeoff, the number of DSP48E1 slices could be significantly reduced with further optimization.

The module runs at the same clock frequency as the ADC and DAC of the WARP board which is 40 MHz. Certainly, one can further enhance the data-rate performance of the module by tuning the clock frequency on the Virtex 6 FPGA, for example, to a maximum of 103 MHz. Once the DPD coefficient α converges, the module introduces a small latency of 13 additional clock cycles for passing the LTE signal from BRAM to PA. This latency accounts for the digital predistortion filtering in (4) using the estimated DPD coefficient α . This low overhead for implementation shows the feasibility of the sub-band DPD for real mobile systems.

VI. CONCLUSION

This paper proposed a new block-adaptive sub-band digital predistortion (DPD) solution for the mitigation of unwanted spurious emissions with spectrally noncontiguous signals and showed real-time prototype implementation results on the WARP platform. The algorithm shows considerable capabilities to suppress the targeted spurious emissions in both simulations and real-time experiments, with greatly reduced computational requirements compared to traditional DPD solutions.

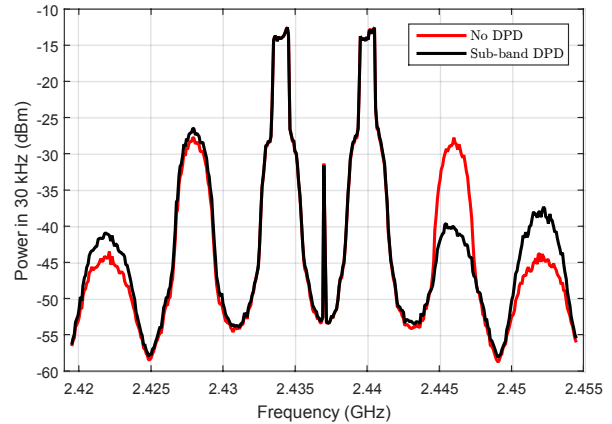


Fig. 10. Spectrum analyzer output with and without DPD in the FPGA design showing approximately 12 dB of suppression at the IM3 sub-band.

In the experimental tests based on WARPLab, the algorithm has been shown to suppress the spurious emissions on the IM3 sub-band by approximately 15 dB. The FPGA implementation of the block based sub-band DPD design can achieve high linearization performance under real-time requirements in a practical transmitter. Many trade-off strategies are considered in the hardware design to balance the robustness, performance and complexity of the proposed sub-band DPD solution.

REFERENCES

- [1] F. M. Ghannouchi and O. Hammi, "Behavioral modeling and predistortion," *IEEE Microw. Mag.*, pp. 52–64, Dec. 2009.
- [2] L. Sundström, A. Walln, and A. Khayrallah, "Carrier aggregation for LTE-advanced: Design challenges of terminals," *IEEE Commun. Mag.*, pp. 76–84, Dec. 2013.
- [3] T. Lähteensuo, "Linearity requirements in LTE Advanced mobile transmitter," M.S. thesis, Tampere University of Technology, Tampere, Finland., May 2013.
- [4] M. Abdelaziz, L. Anttila, A. Mohammadi, F. Ghannouchi, and M. Valkama, "Reduced-complexity power amplifier linearization for carrier aggregation mobile transceivers," in *IEEE International Conference on Acoustics, Speech, and Signal Processing ICASSP*, May 2014.
- [5] M. Abdelaziz, L. Anttila, J.R. Cavallaro, S. Bhattacharyya, A. Mohammadi, F. Ghannouchi, M. Juntti, and M. Valkama, "Low-complexity digital predistortion for reducing power amplifier spurious emissions in spectrally-agile flexible radio," in *9th International Conference on Cognitive Radio Oriented Wireless Networks*, June 2014.
- [6] P. Roblin, S. K. Myoung, D. Chaillot, Y. G. Kim, A. Fathimulla, J. Strahler, and S. Bibyk, "Frequency-selective predistortion linearization of RF power amplifiers," *IEEE Trans. Microw. Theory Tech.*, vol. 56, pp. 65–76, Jan. 2008.
- [7] J. Kim, P. Roblin, D. Chaillot, and Z. Xie, "A generalized architecture for the frequency-selective digital predistortion linearization technique," *IEEE Trans. Microw. Theory Tech.*, vol. 61, pp. 596–605, Jan. 2013.
- [8] S.A. Bassam, M. Helaoui, and F.M. Ghannouchi, "Channel-selective multi-cell digital predistorter for multi-carrier transmitters," *IEEE Trans. Microw. Theory Tech.*, vol. 60, pp. 2344–2352, Aug. 2012.
- [9] A.S. Tehrani, H. Cao, S. Afsardoost, T. Eriksson, M. Isaksson, and C. Fager, "A comparative analysis of the complexity/accuracy tradeoff in power amplifier behavioral models," *IEEE Trans. Microw. Theory Tech.*, vol. 58, pp. 1510–1520, June 2010.
- [10] *International Telecommunication Union Radio Communication Sector, Recommendation ITU-R SM.329-12 Unwanted emissions in the spurious domain*, 2013.
- [11] WARPLab, <http://warpproject.org/trac/wiki/WARPLab>.